

What is the neutral wind in height-integrated ionospheric electrodynamics?

S. M. Hatch¹, J. K. Burchill², H. Vanhamäki³, R. L. A. Mesquita⁴, K. M. Laundal¹, D. J. Knudsen²

¹Department of Physics and Technology, University of Bergen, Bergen, Norway

²Department of Physics and Astronomy, University of Calgary, Calgary, Alberta, Canada

³Space Physics and Astronomy Research Unit, University of Oulu, Oulu, Finland

⁴Johns Hopkins University Applied Physics Laboratory, Laurel, MD, USA

Key Points:

- There is generally no single suitable definition of the neutral wind in height-integrated descriptions of ionosphere-thermosphere dynamics
- The expression $\Sigma_P |\mathbf{E} + \mathbf{U} \times \mathbf{B}|^2$ for height-integrated Joule heating is strictly a lower bound
- The errors that *E*-region wind shears introduce in common expressions for key IT parameters increase with increasing geomagnetic activity

Corresponding author: Spencer Mark Hatch, spencer.hatch@uib.no

Abstract

In most large-scale MHD models of Earth’s space environment, coupling between the magnetosphere and the ionosphere-thermosphere (IT) is addressed by representing the latter as a two-dimensional spherical shell. Similarly, most empirical models of IT electrodynamics are based on solving the height-integrated ionospheric Ohm’s law on a spherical shell. We show that there is in general no single suitable definition of the neutral wind term in high-latitude, height-integrated IT electrodynamics. Instead, two neutral wind terms weighted by Hall and Pedersen conductivities appear. We show that a commonly used expression for Joule heating in terms of height-integrated quantities is a lower bound of the actual Joule heating. Using neutral wind profiles derived from sounding rocket chemical release experiments near Poker Flat, Alaska, and Poker Flat Incoherent Scatter Radar (PFISR) measurements, we find differences of order 10–100 m/s between the two neutral wind terms.

Plain Language Summary

The Earth’s ionosphere at altitudes of ~80 to a few hundred km overlaps with upper atmospheric layer known as the thermosphere. One of the largest challenges facing researchers who are trying to understand how these regions are connected is the fact that it is difficult to make measurements of the atmospheric winds at these altitudes. This is a problem because these winds can vary drastically with altitude. In this study we demonstrate how such variations can make it impossible to faithfully represent the 3D atmospheric winds with a single 2D vector field in 2D representations of ionospheric electrodynamics, and how 2D representations underestimate the atmospheric heating that is caused by friction between charged and neutral particles. We then use radar measurements and rocket-measured altitude profiles of atmospheric winds to estimate how large the errors associated with 2D representations of ionospheric electrodynamics can be.

1 Introduction

Earth’s overlapping ionosphere-thermosphere (IT) region is the site of mechanical and electrodynamic coupling between the neutral atmosphere and plasmas of both terrestrial (magnetospheric and ionospheric) and extraterrestrial (solar wind) origin. Much of the electrodynamics within this region can be described in terms of a three-fluid model consisting of neutral, ion, and electron fluids in the presence of a strong background magnetic field (Section 9.5 in Parker, 2007).

A common point of reference for a vast number of experimental investigations of high-latitude IT electrodynamics is the horizontal component of the ionospheric Ohm’s law assuming steady-state stress balance between Lorentz and collisional drag forces and neglecting all other forces in the ion momentum equation (Section 5 in Chapman, 1956):

$$\mathbf{j}_\perp = \sigma_P (\mathbf{E}_\perp + \mathbf{u} \times \mathbf{B}) + \sigma_H \mathbf{b} \times (\mathbf{E}_\perp + \mathbf{u} \times \mathbf{B}), \tag{1}$$

with σ_P and σ_H Pedersen and Hall conductivities, and \mathbf{E}_\perp , \mathbf{B} , and \mathbf{u} the ionospheric electric field, the total (background plus perturbation) magnetic field, and the neutral wind. The corresponding Joule heating density (heat transfer rate per volume) is given by

$$w_J = \mathbf{j}_\perp \cdot (\mathbf{E}_\perp + \mathbf{u} \times \mathbf{B}) = \sigma_P |\mathbf{E}_\perp + \mathbf{u} \times \mathbf{B}|^2. \tag{2}$$

Both \mathbf{j}_\perp and w_J are independent of reference frame in (magnetic) Galilean relativity (Mannucci et al., 2022) by virtue of the fact that they are defined in terms of the sum of the electric field and the “neutral wind dynamo” $\mathbf{u} \times \mathbf{B}$.

One experimental investigation of Equations 1 and 2 was the Joule II suborbital sounding rocket campaign. Using in situ measurements of electric field, bulk ion drift,

63 and neutral wind in the vicinity of a relatively quiescent auroral breakup in northern Alaska,
 64 Sangalli et al. (2009) reported the errors in E -region ion-neutral momentum transfer col-
 65 lision frequency and Joule heating altitude profiles that would arise if the neutral winds
 66 were assumed to be zero. In a separate analysis of these and additional rocket and ground-
 67 based observations from the same campaign, Burchill et al. (2012) found evidence for
 68 horizontal or vertical structuring in ion-neutral collision frequencies on scales of 1–10 km.

69 Such comprehensive altitude profiles are rare, and instead one frequently encoun-
 70 ters a height-integrated form of the ionospheric Ohm’s law:

$$71 \quad \mathbf{J}_\perp = \Sigma_P (\mathbf{E}_\perp + \mathbf{U} \times \mathbf{B}) + \Sigma_H \mathbf{b} \times (\mathbf{E}_\perp + \mathbf{U} \times \mathbf{B}), \quad (3)$$

72 where Σ_P and Σ_H are the Pedersen and Hall conductances (conductivities integrated
 73 over altitude). This form is obtained by integrating Equation 2 over altitude assuming
 74 that \mathbf{B} is radial, that \mathbf{B} and \mathbf{E}_\perp are independent of altitude over ionospheric E - and F -
 75 region altitudes (~ 100 – 250 km), and that \mathbf{U} is the height-averaged neutral wind or a “rep-
 76 resentative” or “effective” neutral wind at a particular altitude. (The neutral wind \mathbf{U}
 77 in particular is often assumed to be zero in Earth’s rotating frame of reference. A brief
 78 summary of the implications of assuming the E -field is constant with altitude is given
 79 in Text S1 of the Supporting Information.) With these assumptions one may define a
 80 height-integrated Joule heating rate

$$81 \quad W_J = \int w_J dh = \mathbf{J}_\perp \cdot (\mathbf{E}_\perp + \mathbf{U} \times \mathbf{B}) = \Sigma_P (\mathbf{E}_\perp + \mathbf{U} \times \mathbf{B})^2, \quad (4)$$

82 and estimate ionospheric conductances via the expressions

$$83 \quad \Sigma_H = \pm \hat{\mathbf{r}} \cdot [\mathbf{J}_\perp \times (\mathbf{E}_\perp + \mathbf{U} \times \mathbf{B})] / |\mathbf{E}_\perp + \mathbf{U} \times \mathbf{B}|^2; \quad (5)$$

$$84 \quad \Sigma_P = \mathbf{J}_\perp \cdot (\mathbf{E}_\perp + \mathbf{U} \times \mathbf{B}) / |\mathbf{E}_\perp + \mathbf{U} \times \mathbf{B}|^2; \quad (6)$$

85 where the upper and lower signs of the RHS in Equation 5 are respectively for the North-
 86 ern and Southern Hemisphere. The approach represented by Equation 4 to estimating
 87 height-integrated Joule heating dates at least back to the work of Cole (1975) and con-
 88 tinues to be used widely, while the approach to estimating conductances represented by
 89 Equations 5–6 originates with Amm (2001). This approach has been used by a number
 90 of studies over the past two decades, and has elsewhere been referred to as the “elemen-
 91 tary current method” or the “electrodynamic method” (e.g., Amm, 2001; Green et al.,
 92 2007; Weimer & Edwards, 2021; Hatch et al., 2023).

93 The height-integrated approach to ionospheric electrostatics represented by Equa-
 94 tions 3–6 is oversimplified: Earth’s magnetic field lines are not radial, ionospheric elec-
 95 tric fields do not necessarily map along field lines (Farley, 1959), and the horizontal com-
 96 ponents of the neutral wind exhibit the nearly permanent presence of vertical shears over
 97 altitudes of 80 to 140 km (Heppner & Miller, 1982; Larsen, 2002; Sangalli et al., 2009).
 98 More advanced treatments of ionospheric electrostatics that account for such com-
 99 plications, such as that presented by Richmond (1995), nevertheless remain unused in
 100 a large number of experimental studies and data assimilation techniques (e.g., Richmond
 101 & Kamide, 1988; Matsuo, 2020; Laundal et al., 2022) because we lack the body of ro-
 102 bust 3D measurements of the IT system needed to make use of them (Palmroth et al.,
 103 2021). For similar reasons, in the majority of existing global MHD models the coupling
 104 between the magnetosphere and the IT system is founded on what Mannucci et al. (2022)
 105 term a “key magnetosphere-ionosphere coupling equation” derived from current conti-
 106 nuity (their Equation 11; see also Merkin & Lyon, 2010; Mukhopadhyay et al., 2021, and
 107 references therein) in which the neutral wind is assumed to be zero or constant with al-
 108 titude.

109 In this study, we explore some of the implications of the commonly employed as-
 110 sumption that the neutral wind is independent of altitude that is necessary to arrive at

111 Equations 3–6 and the current continuity equation used in magnetosphere-ionosphere
 112 coupling. In Section 2 we summarize central quantities and equations in a height-integrated
 113 description of IT electrodynamics when the neutral wind is not assumed to be indepen-
 114 dent of altitude. In Section 3 we present neutral wind profiles derived from rocket-borne
 115 trimethylaluminum (TMA) chemical release experiments launched from the Poker Flat
 116 Research Range (PFRR) between 2007 and 2018 together with conductivity profiles cal-
 117 culated from measurements made by the Poker Flat Incoherent Scatter Radar (PFISR),
 118 and use these to understand how the assessment of the local IT electrodynamics is mod-
 119 ified by assuming the neutral wind is independent of altitude. In Section 4 we summa-
 120 rize our findings.

121 2 Defining the neutral wind in height-integrated IT electrodynamics

122 Relaxing the assumption that \mathbf{u} does not vary with height, integration of Ohm’s
 123 law (Equation 1) over ionospheric altitudes yields

$$124 \quad \mathbf{J}_\perp = \Sigma_P \mathbf{F}_P + \Sigma_H \hat{\mathbf{b}} \times \mathbf{F}_H = \Sigma_P \mathbf{F}_P + \Sigma_H \hat{\mathbf{b}} \times \mathbf{F}_P + \Sigma_H \hat{\mathbf{b}} \times (\mathbf{U}_H - \mathbf{U}_P) \times \mathbf{B}, \quad (7)$$

125 where

$$126 \quad \mathbf{F}_c = \mathbf{E}_\perp + \mathbf{U}_c \times \mathbf{B}; \quad (8)$$

$$127 \quad \mathbf{U}_c = \frac{1}{\Sigma_c} \int \sigma_c \mathbf{u} dh; \quad (9)$$

128 and c is either H or P . The integration is performed over all ionospheric altitudes. We
 129 refer to the conductivity-weighted neutral wind terms \mathbf{U}_H and \mathbf{U}_P as the Hall-weighted
 130 or Pedersen-weighted neutral winds. The latter has been termed the “effective neutral
 131 wind” by Lu et al. (1995) and plays a role in estimates of height-integrated Joule heat-
 132 ing and the Pedersen conductance, which we discuss below. The distinction between the
 133 Hall-weighted and Pedersen-weighted neutral winds disappears when the two conduc-
 134 tivity profiles differ by no more than a constant factor, or when the neutral wind \mathbf{u} does
 135 not vary with altitude. As noted in the Introduction, these idealized conditions are vir-
 136 tually never manifest in measured altitude profiles of the neutral winds.

137 Taking the dot product of Equation 7 with \mathbf{F}_P yields

$$138 \quad \mathbf{J}_\perp \cdot \mathbf{F}_P = \Sigma_P F_P^2 + M \Sigma_H, \quad (10)$$

139 where

$$140 \quad M = B [\mathbf{E}_\perp \cdot (\mathbf{U}_H - \mathbf{U}_P) + \mathbf{B} \cdot (\mathbf{U}_H \times \mathbf{U}_P)]. \quad (11)$$

141 The radial component of the cross product of Equation 7 with \mathbf{F}_H is

$$142 \quad \hat{\mathbf{r}} \cdot (\mathbf{J}_\perp \times \mathbf{F}_H) = \pm \Sigma_H F_H^2 \pm M \Sigma_P, \quad (12)$$

143 with the upper sign for the Northern Hemisphere.

144 Equations 10 and 12 can be simultaneously solved to obtain generalizations of Equa-
 145 tions 5 and 6 for height-integrated conductances in terms of the Hall-weighted and Pedersen-
 146 weighted neutral winds:

$$147 \quad \Sigma_H = \frac{\pm |\mathbf{F}_P^2| \hat{\mathbf{r}} \cdot (\mathbf{J}_\perp \times \mathbf{F}_H) - M \mathbf{J}_\perp \cdot \mathbf{F}_P}{|\mathbf{F}_H^2| |\mathbf{F}_P^2| - M^2}; \quad (13)$$

$$148 \quad \Sigma_P = \frac{\mathbf{J}_\perp \cdot \mathbf{F}_P}{|\mathbf{F}_P|^2} \left(1 + \frac{M^2}{|\mathbf{F}_H|^2 |\mathbf{F}_P|^2 - M^2} \right) \mp M \frac{\hat{\mathbf{r}} \cdot (\mathbf{J}_\perp \times \mathbf{F}_H)}{|\mathbf{F}_H|^2 |\mathbf{F}_P|^2 - M^2}. \quad (14)$$

149 When $\mathbf{U}_H = \mathbf{U}_P$ we have $M = 0$, and Equations 13 and 14 reduce to the expressions
 150 for Hall and Pedersen conductances given by Equations 5 and 6.

151 Integrating the right-hand side of the expression for Joule heating density (2), we
 152 obtain

$$W_J = \Sigma_P [E_{\perp}^2 + 2\mathbf{E}_{\perp} \cdot (\mathbf{U}_P \times \mathbf{B})] + \int \sigma_P \|\mathbf{u} \times \mathbf{B}\|^2 dh. \quad (15)$$

153 This expression cannot directly be brought into the more familiar form $\Sigma_P (\mathbf{E}_{\perp} + \mathbf{U} \times \mathbf{B})^2$
 154 for some appropriately chosen \mathbf{U} (cf. Equation 4) because of the integral in the last term.
 155 However, one may show explicitly via the Cauchy-Bunyakovsky-Schwarz inequality that
 156 $\int \sigma_P \|\mathbf{u} \times \mathbf{B}\|^2 dh \geq \Sigma_P (\mathbf{U}_P \times \mathbf{B})^2$ (see Text S2 in Supporting Information). Then the
 157 following inequalities hold:

$$\begin{aligned} W_J &\geq \Sigma_P (\mathbf{E}_{\perp} + \mathbf{U}_P \times \mathbf{B})^2 = \Sigma_P \mathbf{F}_P^2; \\ \Sigma_P &\leq W_J / \mathbf{F}_P^2. \end{aligned} \quad (16)$$

159 Thus when the variable \mathbf{U} is replaced with \mathbf{U}_P in Equations 4 and 6, these equations
 160 are in fact lower and upper bounds, respectively, on the true height-integrated Joule heat-
 161 ing and Pedersen conductance. When the neutral wind does not vary with altitude we
 162 have $\mathbf{U}_P \rightarrow \mathbf{U}$ in Inequality 16, such that the height-integrated Joule heating $W_J =$
 163 $\Sigma_P (\mathbf{E} + \mathbf{U} \times \mathbf{B})^2$ and the Pedersen conductance $\Sigma_P = W_J / (\mathbf{E} + \mathbf{U} \times \mathbf{B})^2$ as given by
 164 Equations 4 and 6.

165 From the foregoing we see that for estimation of height-integrated Joule heating
 166 and the Pedersen conductance, the Pedersen-weighted neutral wind \mathbf{U}_P constitutes the
 167 most natural definition of the “effective” neutral wind, as indirectly suggested by Lu et
 168 al. (1995).

169 **3 Experimental examination of Hall- and Pedersen-weighted neutral** 170 **winds**

171 Section 2 illustrates that it is in general not possible to uniquely define the neu-
 172 tral wind term in height-integrated (or for that matter field line-integrated) treatments
 173 of IT electrodynamics. Instead, the neutral wind appears as two separate terms weighted
 174 separately by the Hall and Pedersen conductivity profiles, here defined by Equation 9
 175 and respectively denoted by \mathbf{U}_H and \mathbf{U}_P . This situation begs the following questions:

- 176 1. How large is the observed difference between \mathbf{U}_H and \mathbf{U}_P ?
- 177 2. How much better are various rule-of-thumb approximations for the neutral wind
 178 (e.g., the suggestion from Lu et al., 1995, that the “winds at 160 km” are repre-
 179 sentative of the “effective neutral wind”) than simply assuming $\mathbf{U}_H = \mathbf{U}_P =$
 180 $\mathbf{u} = 0$?
- 181 3. Are the differences between \mathbf{U}_H and \mathbf{U}_P meaningful for assessments of IT elec-
 182 trodynamics?

183 To answer these questions we use horizontal neutral wind profiles derived from TMA
 184 chemical release experiments carried by sounding rockets during five campaigns launched
 185 from the Poker Flat Research Range (Mesquita, 2021, and references therein), as well
 186 as conductivity profiles derived from Poker Flat Incoherent Scatter Radar (PFISR) mea-
 187 surements and empirical models of ionospheric and atmospheric composition, atmospheric
 188 temperature, and Earth’s magnetic field.

189 **3.1 Measurements and models**

190 Figure 1 shows a summary of the 15 wind profiles used in this study, with the zonal
 191 and meridional components displayed respectively in the left and center columns, and
 192 the horizontal magnitudes in the right column. The vertical component is not estimated
 193 and is ignored throughout this study. The text label at right shows the date, campaign
 194 name, and Kp value for each group of wind profiles. The chronological ordering of the

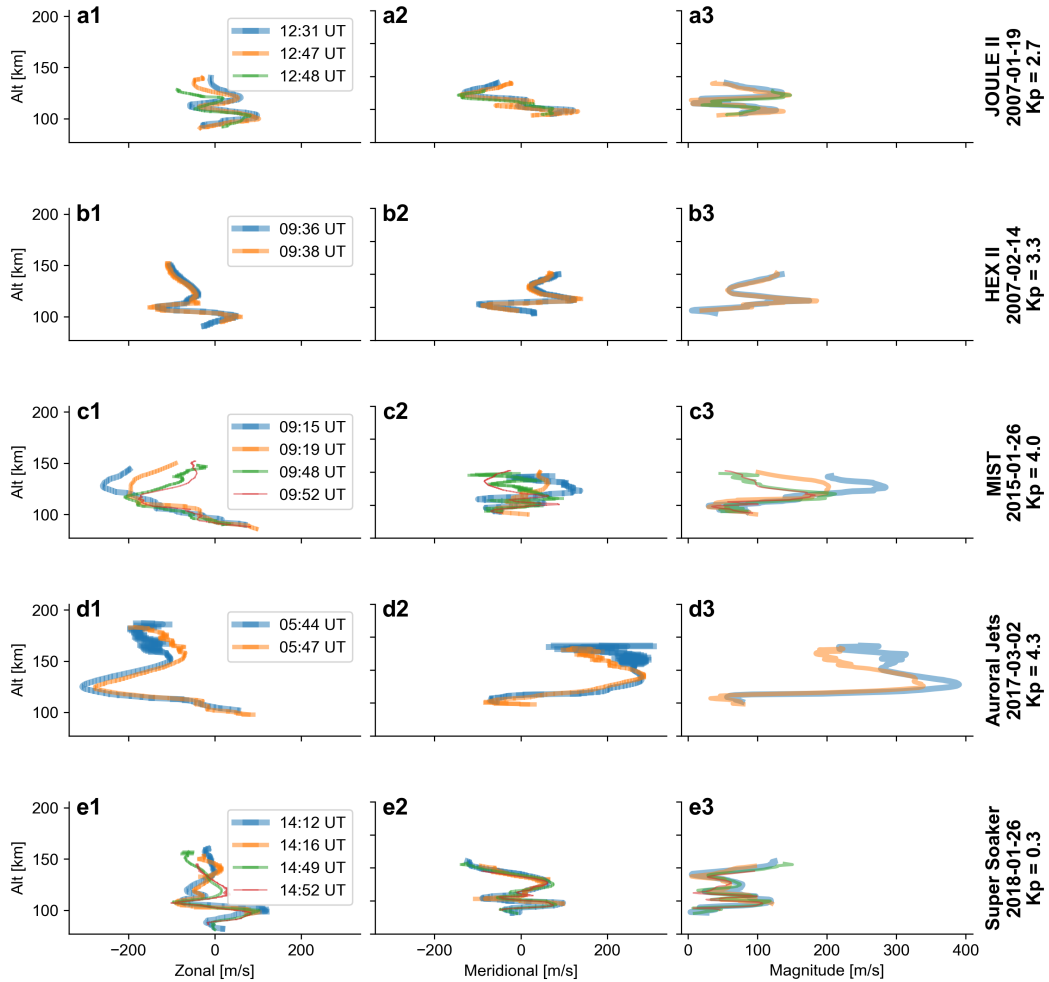


Figure 1. Summary of neutral wind profiles used in this study, given in the same order as the rocket campaigns in Table S1 in the Supporting Information. The zonal and meridional components are shown in the left and center columns, with the magnitude profiles shown in the right column. The campaign name and degree of geomagnetic activity are indicated in the caption at far right in each row.

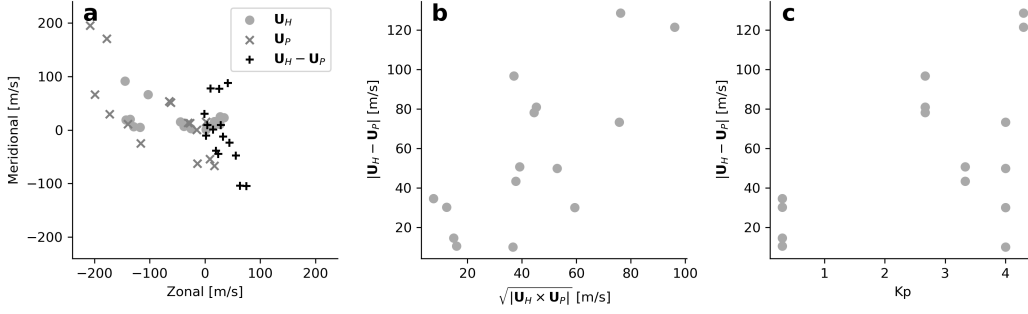


Figure 2. (a) Statistics of \mathbf{U}_H , \mathbf{U}_P , $\mathbf{U}_H - \mathbf{U}_P$. (b) The magnitude of the difference of \mathbf{U}_H and \mathbf{U}_P against the square root of the magnitude of their cross product. (c) The magnitude of the difference of \mathbf{U}_H and \mathbf{U}_P against Kp. This figure answers Question 1 posed at the beginning of Section 3 (“How large is the observed difference between \mathbf{U}_H and \mathbf{U}_P ?”), and gives an impression of the typical magnitudes of these quantities, which appear in Equations 10–12.

195 rows of Figure 1 coincidentally also orders the wind profiles by Kp, aside from the last
 196 row (Super Soaker campaign) for which Kp was lowest (Kp= 0.3). The magnitudes of
 197 the wind profiles show a clear tendency to increase with increasing Kp. Some details about
 198 each campaign, including the time of each measurement (center time of images used for
 199 triangulation) and the availability of PFISR measurements, are given in Table S1 of the
 200 Supporting Information.

201 For each wind profile shown in Figure 1 we calculate corresponding \mathbf{U}_H and \mathbf{U}_P
 202 vectors via Equation 9. This calculation in turn requires calculation of conductivity pro-
 203 files, which we perform using Poker Flat Incoherent Scatter Radar (PFISR) measure-
 204 ments, the NRLMSIS®2.0 empirical atmospheric model (Emmert et al., 2020), and the
 205 International Reference Ionosphere (IRI) 2016 model (Bilitza et al., 2017), following the
 206 methodology of Ieda (2020). The steps of this process are summarized and illustrated
 207 in Text S3 and Figure S1 of the Supporting Information.

208 3.2 Statistics of \mathbf{U}_H and \mathbf{U}_P

209 After performing the procedure described in the previous subsection for all 15 neu-
 210 tral wind profiles, we obtain the estimates of \mathbf{U}_H and \mathbf{U}_P as well as their difference ($\mathbf{U}_H -$
 211 \mathbf{U}_P) shown in Figure 2a. For these neutral wind profiles the zonal component of \mathbf{U}_H and
 212 \mathbf{U}_P exhibits a tendency to be negative (westward), while the meridional components ex-
 213 hibit a slight tendency to be positive (northward). The magnitudes of \mathbf{U}_H and \mathbf{U}_P
 214 are of order 10–100 m/s, with the magnitude of the former tending to be the smaller of the
 215 two. Given the magnitude of the geomagnetic field at PFRR ($\sim 54,000$ nT at 110-km al-
 216 titude), these magnitudes correspond to electric field equivalents of ~ 0.5 –5 mV/m.

217 We do not attempt to draw general conclusions about \mathbf{U}_H and \mathbf{U}_P on the basis
 218 of the estimates shown in Figure 2a, as they are representative of only one location (PFRR)
 219 for a sparsely sampled range of universal times (~ 06 –14 UT) and one season (January
 220 to March), as indicated in Table S1 of the Supporting Information. It nevertheless seems
 221 probable that the range of magnitudes of \mathbf{U}_H and \mathbf{U}_P shown in Figure 2a is typical at
 222 high latitudes during low to moderate geomagnetic activity.

223 Figure 2b plots $|\mathbf{U}_H - \mathbf{U}_P|$ against the magnitude of their cross product. The mag-
 224 nitudes of these two quantities are relevant to examine as they both appear in Equations 10
 225 and 12. From values in this panel we see that the typical magnitude of “mismatch” be-

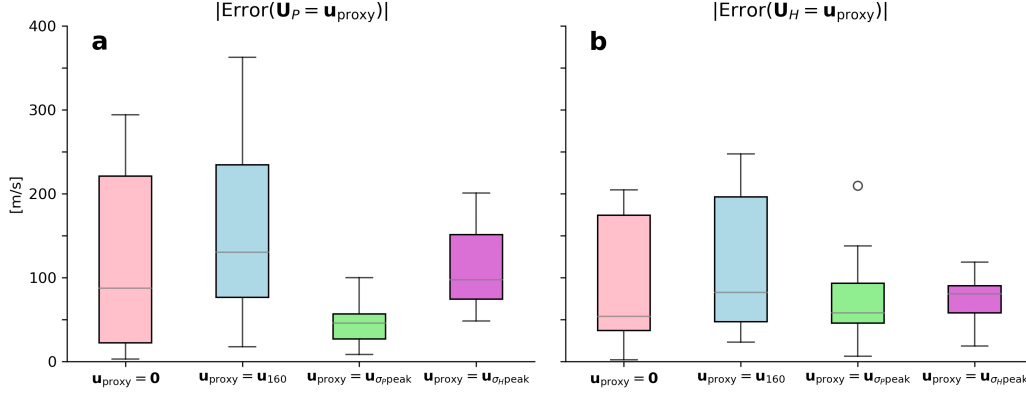


Figure 3. (a) For 15 neutral wind profiles, statistics of the magnitude of the Pedersen-weighted neutral wind (\mathbf{U}_P , pink), the magnitude of the differences between \mathbf{U}_P and the neutral wind at 160-km altitude (\mathbf{u}_{160} , blue), the magnitude of the difference between \mathbf{U}_P and the neutral wind at the height at which the Pedersen conductance maximizes ($\mathbf{u}_{\sigma_P \text{ peak}}$, green), and the magnitude of the difference between \mathbf{U}_P and the neutral wind at the height at which the Hall conductance maximizes ($\mathbf{u}_{\sigma_H \text{ peak}}$, violet). The first and second represent the error associated with assuming $\mathbf{U}_P = 0$ m/s and $\mathbf{U}_P = \mathbf{u}_{160}$; the latter two represent the error associated with assuming \mathbf{U}_P is one of the two proxies. The horizontal lines above and below each box plot are respectively given by $Q3 + 1.5\text{IQR}$ and $Q1 - 1.5\text{IQR}$ (see main text). (b) Same as panel a, but for the Hall-weighted neutral wind \mathbf{U}_H . The point of this figure is to answer Question 2 posed at the beginning of Section 3 by assessing whether any proxy for the Hall- and Pedersen-weighted neutral winds statistically incurs less error than simply assuming that they are zero.

226 between \mathbf{U}_H and \mathbf{U}_P is $\sim 5\text{--}130$ m/s. It is also evident that the quantities $|\mathbf{U}_H - \mathbf{U}_P|$ and
 227 $|\mathbf{U}_H \times \mathbf{U}_P|$ are positively correlated.

228 Figure 2c plots $|\mathbf{U}_H - \mathbf{U}_P|$ against the Kp value during each rocket launch, with
 229 the former tending to be smallest for low Kp and the degree of scatter increasing for in-
 230 creasing Kp.

231 3.3 Proxies for the Hall- and Pedersen-weighted neutral winds

232 Here we address Question 2 posed at the beginning of this section: How much bet-
 233 ter are various rule-of-thumb approximations for the neutral wind than simply assum-
 234 ing $\mathbf{U}_H = \mathbf{U}_P = \mathbf{u} = 0$? To answer this question, Figure 3a shows the error distri-
 235 bution $\text{Error}(\mathbf{U}_P = \mathbf{u}_{\text{proxy}}) = |\mathbf{U}_P - \mathbf{u}_{\text{proxy}}|$ associated with the assumption $\mathbf{U}_P =$
 236 $\mathbf{u}_{\text{proxy}}$, where $\mathbf{u}_{\text{proxy}}$ is taken to be one of $\mathbf{0}$, \mathbf{u}_{160} , $\mathbf{u}_{\sigma_P \text{ peak}}$, or $\mathbf{u}_{\sigma_H \text{ peak}}$. These are respec-
 237 tively the zero vector, the neutral wind at 160-km altitude, the neutral wind at the alti-
 238 tude where the Pedersen conductivity profile peaks, and the neutral wind at the alti-
 239 tude where the Hall conductivity profile peaks. Each distribution is presented as a ver-
 240 tical box plot, where each box indicates (from top to bottom) the upper quartile $Q3$, the
 241 median, and lower quartile $Q1$. The horizontal lines above and below are respectively
 242 given by $Q3 + 1.5\text{IQR}$ and $Q1 - 1.5\text{IQR}$, where $\text{IQR} = Q3 - Q1$ is the interquartile
 243 range. In analogy with Figure 3a, Figure 3b shows the error associated with assuming
 244 $\mathbf{U}_H = \mathbf{u}_{\text{proxy}}$.

245 Figure 3a demonstrates that for the 15 neutral wind profiles examined in this study,
 246 assuming $\mathbf{U}_P = \mathbf{u}_{\sigma_P \text{ peak}}$ statistically incurs less error than assuming $\mathbf{U}_P = \mathbf{0}$, $\mathbf{U}_P =$

247 \mathbf{u}_{160} , or $\mathbf{U}_P = \mathbf{u}_{\sigma_H \text{peak}}$. For \mathbf{U}_H , Figure 3b shows that assuming $\mathbf{U}_H = \mathbf{0}$ incurs the
 248 least median error of any proxy, although the overall range of errors is smallest for $\mathbf{U}_H =$
 249 $\mathbf{u}_{\sigma_H \text{peak}}$.

250 In the simulations that Lu et al. (1995) presented, they found that the “effective
 251 neutral wind pattern” (what we term the Pedersen-weighted neutral wind \mathbf{U}_P) is equiv-
 252 alent to the neutral wind pattern at 160-km altitude. This rule of thumb has been em-
 253 ployed by Baker et al. (2004) and Billett et al. (2018). Figure 3a shows that for the ma-
 254 jority of the 15 neutral wind profiles examined in this study, this rule of thumb yields
 255 a larger error than the more naïve assumption that $\mathbf{u} = \mathbf{0}$.

256 4 Discussion

257 Lu et al. (1995), Baker et al. (2004), and Billett et al. (2018) all make use of the
 258 idea of a two-dimensional “effective neutral wind” pattern. As we have shown in Sec-
 259 tion 2, the most suitable definition for the “effective neutral wind” in terms of smallest
 260 error incurred is what we have termed the Pedersen-weighted neutral wind \mathbf{U}_P given in
 261 Equation 9. Based on Lu et al. (1995), the latter two pick up on the idea of the neutral
 262 winds at 160-km altitude as being the “effective” altitude.

263 Regarding Question 3 posed at the beginning of Section 3—whether the observed
 264 differences between \mathbf{U}_H and \mathbf{U}_P are meaningful for assessments of IT electrodynamics—
 265 we get some idea of the importance of the distinction between them by examining the
 266 magnitude of the quantity $\mathbf{B}\mathbf{B}\cdot(\mathbf{U}_H \times \mathbf{U}_P)$ in the expression for M given by Equation 11.
 267 This quantity appears in the expressions 13 and 14 for height-integrated conductances
 268 when the distinction between \mathbf{U}_H and \mathbf{U}_P is maintained. From Figure 2, we have $|\mathbf{U}_H \times$
 269 $\mathbf{U}_P| \sim \mathcal{O}(10^2\text{--}10^4)$ (m/s)² such that $\sqrt{|\mathbf{B}\mathbf{B}\cdot(\mathbf{U}_H \times \mathbf{U}_P)|} \sim \mathcal{O}(0.5\text{--}5)$ mV/m. This
 270 makes clear that ignoring the distinction between \mathbf{U}_H and \mathbf{U}_P can incur a non-negligible
 271 error in estimation of Σ_H and Σ_P , even when the “effective neutral wind” \mathbf{U}_P is used
 272 in Equations 5–6 for height-integrated conductance. With the present severe lack of sys-
 273 tematic measurements of the neutral wind, this result underscores the difficult situation
 274 facing studies such as those of Weimer and Edwards (2021) and Hatch et al. (2023), in
 275 which the authors attempt to estimate Σ_H and Σ_P on the basis of Equations 5–6 assum-
 276 ing $\mathbf{u} = \mathbf{0}$: in a number of scenarios where one wishes to represent high-latitude IT elec-
 277 trodynamics in two dimensions, one misses potentially important aspects of this coupling
 278 by representing the neutral wind with a single variable.

279 In the context of Question 3 it is also relevant to compare the neutral wind term
 280 $\Sigma_P|\mathbf{U}_P \times \mathbf{B}|^2$ with the explicitly height-integrated term $\int \sigma_P|\mathbf{u} \times \mathbf{B}|^2 dh$ in Equation 15,
 281 as discussed in Section 2. Figure 4 shows that the former underestimates the latter by
 282 9–96%, with the magnitude of underestimation decreasing as $\int \sigma_P|\mathbf{u} \times \mathbf{B}|^2 dh$ increases,
 283 and the gap between $\Sigma_P|\mathbf{U}_P \times \mathbf{B}|^2$ and $\int \sigma_P|\mathbf{u} \times \mathbf{B}|^2 dh$ tending to decrease with increas-
 284 ing Kp.

285 The results in Section 2 have some bearing on the “key MI coupling equation” de-
 286 rived from current continuity that is mentioned in the introduction,

$$287 \quad \nabla \cdot \mathbf{J}_\perp = -j_\parallel, \quad (17)$$

288 where the integrated perpendicular current \mathbf{J}_\perp is given by a height- or field line-integrated
 289 form of Ohm’s law (i.e., $\mathbf{J}_\perp = \bar{\bar{\Sigma}} \cdot [\mathbf{E}_\perp + \mathbf{U} \times \mathbf{B}]$) in terms of the potential electric field
 290 $\mathbf{E}_\perp = -\nabla_\perp \Phi$ and the ionospheric conductance tensor $\bar{\bar{\Sigma}}$. The development in Section 2
 291 shows that it is strictly speaking not possible to formulate the height-integrated iono-
 292 spheric Ohm’s law as given by Equation 7 in terms of the conductance tensor $\bar{\bar{\Sigma}}$, because
 293 \mathbf{F}_H and \mathbf{F}_P are generally not identical. It is unclear from the results presented in Fig-
 294 ure 3 how much the differences between \mathbf{U}_H and \mathbf{U}_P can affect the description of IT elec-
 295 trodynamics in models that employ some form of this equation. What is true statisti-

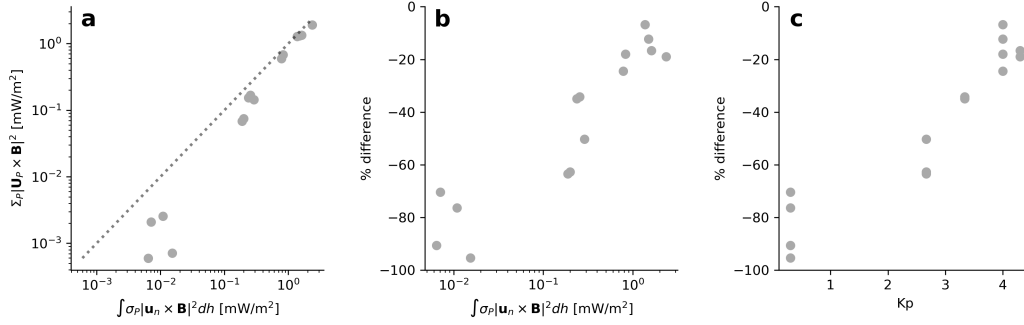


Figure 4. (a) Comparison of the difference between the height-integrated neutral wind term $\int \sigma_P |\mathbf{u} \times \mathbf{B}|^2 dh$ (last term on RHS of Equation 15) and the lower-bound approximation $\Sigma_P |\mathbf{U}_P \times \mathbf{B}|^2$. (b) Percent difference between these quantities relative to $\int \sigma_P |\mathbf{u} \times \mathbf{B}|^2 dh$. (c) Percent difference as a function of Kp. The point of this figure is to assess how much the lower-bound approximation underestimates the magnitude of the integral $\int \sigma_P |\mathbf{u} \times \mathbf{B}|^2 dh$.

296 cally is that the magnitude of the difference between the Hall-weighted and Pedersen-
 297 weighted neutral wind terms tends to increase with increasing geomagnetic activity (Fig-
 298 ure 2c), where in this study the latter is measured by the Kp index.

299 Regarding MI coupling in global models, it is relevant to observe that Equation 17
 300 is not the state of the art: ionosphere-thermosphere models such as the Whole Atmo-
 301 sphere Community Climate Model With Thermosphere and Ionosphere Extension (WACCM-
 302 X, Liu et al., 2018) and the Thermosphere-Ionosphere-Electrodynamics General Circu-
 303 lation Model (Qian et al., 2014) use the 2D continuity equation given in the more ad-
 304 vanced treatment of Richmond (1995). The Richmond (1995) equation generalizes Equa-
 305 tion 17 and does, in fact, take stock of the three-dimensional nature of the neutral wind
 306 field.

307 In one sense this study is only one more voice in the chorus of recent literature call-
 308 ing for additional neutral wind measurements (Sarris, 2019; Heelis & Maute, 2020; Palm-
 309 roth et al., 2021; Dhadly et al., 2023). On the other hand, this study points out a fun-
 310 damental limitation of 2D descriptions of IT electrodynamic: Even when an appropri-
 311 ately defined neutral wind term is used (the Pedersen-weighted neutral wind), any es-
 312 timate of height-integrated Joule heating on the basis of height-integrated and averaged
 313 quantities is mathematically guaranteed to be a lower bound of the actual height-integrated
 314 Joule heating, with some tendency for the pure neutral wind term to be less strongly un-
 315 derestimated with increasing Kp.

316 Regarding our finding in Section 3.3 and Figure 3 that the assumption $\mathbf{u} = 0$ is
 317 statistically a better estimate for both \mathbf{U}_H and \mathbf{U}_P than the neutral winds at 160-km
 318 altitude, \mathbf{u}_{160} , this study deals with a limited selection of neutral wind profiles at one
 319 geographical location and over a limited range of altitudes. The lack of statistics pre-
 320 cludes drawing general conclusions. Our results do nevertheless indicate that one should
 321 be skeptical of “quick fixes” for the neutral wind problem, such as ignoring the winds
 322 or representing them with proxies. Figure 3 also suggests that the assumption $\mathbf{U}_H =$
 323 $\mathbf{U}_P = \mathbf{u}_{\sigma_P, \text{peak}}$ is likely an improvement over simply assuming $\mathbf{U}_H = \mathbf{U}_P = \mathbf{u} = 0$.
 324 This points to the utility of techniques and measurements involving, for example, Doppler
 325 spectroscopy which in some conditions enable estimation of the neutral wind profiles over
 326 limited ranges of altitudes between 120 and 200 km where the Pedersen conductivity pro-
 327 file may peak (Branning et al., 2022; Dhadly et al., 2023).

Open Research Section

The NRLMSIS®2.0, IRI 2016, and IGRF-13 models are respectively queried via the `nrlmsis2.0` (Hirsch, 2020), `iri2016` (Hirsch, 2018), and `ppigrf` (Laundal, 2023) Python packages. Scripts and data used to make the plots shown in this study are available at Zenodo (Hatch & Mesquita, 2024).

Acknowledgments

This study is supported as part of Swarm Data, Innovation, and Science Cluster (DISC) activities, and is funded by ESA contract no. 4000109587/13/I-NB. SMH and KML were also supported by the Trond Mohn Research Foundation. SMH was additionally supported by the Research Council of Norway, contract 344061. KML was additionally supported by the European Union (ERC, DynaMIT, 101086985), and the Research Council of Norway, contract 300844/F50. JKB was supported with funding from Canadian Space Agency grant 15SUSWARM. HV is supported by the Academy of Finland project 354521. RM was supported with funding from NASA Grant with contract number 80NSSC23K0094. The authors thank A. Bhatt (SRI) for helpful guidance regarding the use of PFISR data.

References

- Amm, O. (2001, nov). The elementary current method for calculating ionospheric current systems from multisatellite and ground magnetometer data. *Journal of Geophysical Research: Space Physics*, *106*(A11), 24843–24855. Retrieved from <https://doi.org/10.1029/2001JA900021> <http://doi.wiley.com/10.1029/2001JA900021> doi: 10.1029/2001JA900021
- Baker, J. B. H., Zhang, Y., Greenwald, R. A., Paxton, L. J., & Morrison, D. (2004, may). Height-integrated Joule and auroral particle heating in the night side high latitude thermosphere. *Geophysical Research Letters*, *31*(9). Retrieved from <http://doi.wiley.com/10.1029/2004GL019535> doi: 10.1029/2004GL019535
- Bilitza, D., Altadill, D., Truhlik, V., Shubin, V., Galkin, I., Reinisch, B., & Huang, X. (2017, 2). International reference ionosphere 2016: From ionospheric climate to real-time weather predictions. *Space Weather*, *15*, 418–429. doi: 10.1002/2016SW001593
- Billett, D. D., Grocott, A., Wild, J. A., Walach, M.-T., & Kosch, M. J. (2018, mar). Diurnal Variations in Global Joule Heating Morphology and Magnitude Due To Neutral Winds. *Journal of Geophysical Research: Space Physics*, *123*, 2398–2411. Retrieved from <http://doi.wiley.com/10.1002/2017JA025141> doi: 10.1002/2017JA025141
- Branning, K., Conde, M., Larsen, M., & Troyer, R. (2022, 5). Resolving vertical variations of horizontal neutral winds in earth’s high latitude space-atmosphere interaction region (sair). *Journal of Geophysical Research: Space Physics*, *127*. doi: 10.1029/2021JA029805
- Burchill, J. K., Clemmons, J. H., Knudsen, D. J., Larsen, M., Nicolls, M. J., Pfaff, R. F., ... Sangalli, L. (2012, 2). High-latitude e region ionosphere-thermosphere coupling: A comparative study using in situ and incoherent scatter radar observations. *Journal of Geophysical Research: Space Physics*, *117*. doi: 10.1029/2011JA017175
- Chapman, S. (1956, aug). The electrical conductivity of the ionosphere: A review. *Il Nuovo Cimento*, *4*(S4), 1385–1412. Retrieved from <http://link.springer.com/10.1007/BF02746310> doi: 10.1007/BF02746310
- Cole, K. (1975, jun). Energy deposition in the thermosphere caused by the solar wind. *Journal of Atmospheric and Terrestrial Physics*, *37*(6-7), 939–949. Retrieved from <https://linkinghub.elsevier.com/retrieve/pii/0021916975900082> doi: 10.1016/0021-9169(75)90008-2

- 379 Dhadly, M., Sassi, F., Emmert, J., Drob, D., Conde, M., Wu, Q., ... Nicholas, A.
380 (2023, 1). Neutral winds from mesosphere to thermosphere—past, present,
381 and future outlook. *Frontiers in Astronomy and Space Sciences*, 9. doi:
382 10.3389/fspas.2022.1050586
- 383 Emmert, J. T., Drob, D. P., Picone, J. M., Siskind, D. E., Jones, M., Mlynczak,
384 M. G., ... Yuan, T. (2020, sep). NRLMSIS 2.0: A whole-atmosphere em-
385 pirical model of temperature and neutral species densities. *Earth and Space*
386 *Science*. Retrieved from [https://onlinelibrary.wiley.com/doi/10.1029/](https://onlinelibrary.wiley.com/doi/10.1029/2020EA001321)
387 [2020EA001321](https://onlinelibrary.wiley.com/doi/10.1029/2020EA001321) doi: 10.1029/2020EA001321
- 388 Farley, D. T. (1959, 9). A theory of electrostatic fields in a horizontally stratified
389 ionosphere subject to a vertical magnetic field. *Journal of Geophysical Re-*
390 *search*, 64, 1225-1233. Retrieved from [http://doi.wiley.com/10.1029/](http://doi.wiley.com/10.1029/JZ064i009p01225)
391 [JZ064i009p01225](http://doi.wiley.com/10.1029/JZ064i009p01225) doi: 10.1029/JZ064i009p01225
- 392 Green, D. L., Waters, C. L., Korth, H., Anderson, B. J., Ridley, A. J., & Barnes,
393 R. J. (2007, may). Technique: Large-scale ionospheric conductance estimated
394 from combined satellite and ground-based electromagnetic data. *Journal*
395 *of Geophysical Research: Space Physics*, 112(A5). Retrieved from [http://](http://doi.wiley.com/10.1029/2006JA012069)
396 doi.wiley.com/10.1029/2006JA012069 doi: 10.1029/2006JA012069
- 397 Hatch, S. M., & Mesquita, R. L. A. (2024, April). *Resource for Hatch et al (2024),*
398 *"What is the neutral wind in height-integrated electrodynamics?"*. Zen-
399 odo. Retrieved from <https://doi.org/10.5281/zenodo.11091983> doi:
400 10.5281/zenodo.11091983
- 401 Hatch, S. M., Vanhamäki, H., Laundal, K. M., Reistad, J. P., Burchill, J., Lo-
402 midze, L., ... Tesfaw, H. (2023). Does high-latitude ionospheric electro-
403 dynamics exhibit hemispheric mirror symmetry? *EGUsphere*, 2023, 1–41.
404 Retrieved from [https://egusphere.copernicus.org/preprints/2023/](https://egusphere.copernicus.org/preprints/2023/egusphere-2023-2920/)
405 [egusphere-2023-2920/](https://egusphere.copernicus.org/preprints/2023/egusphere-2023-2920/) doi: 10.5194/egusphere-2023-2920
- 406 Heelis, R., & Maute, A. (2020, 2). Challenges to understanding the earth's iono-
407 sphere and thermosphere. *Journal of Geophysical Research: Space Physics*.
408 Retrieved from [https://onlinelibrary.wiley.com/doi/abs/10.1029/](https://onlinelibrary.wiley.com/doi/abs/10.1029/2019JA027497)
409 [2019JA027497](https://onlinelibrary.wiley.com/doi/abs/10.1029/2019JA027497) doi: 10.1029/2019JA027497
- 410 Heppner, J. P., & Miller, M. L. (1982, mar). Thermospheric winds at high lati-
411 tudes from chemical release observations. *Journal of Geophysical Research:*
412 *Space Physics*, 87(A3), 1633–1647. Retrieved from [http://doi.wiley.com/](http://doi.wiley.com/10.1029/JA087iA03p01633)
413 [10.1029/JA087iA03p01633](http://doi.wiley.com/10.1029/JA087iA03p01633) doi: 10.1029/JA087iA03p01633
- 414 Hirsch, M. (2018). *iri2016*. <https://doi.org/10.5281/zenodo.240895>. doi: 10.5281/
415 zenodo.240895
- 416 Hirsch, M. (2020). *nrlmsis2.0*. <https://github.com/space-physics/nrlmsis2.0>.
- 417 Ieda, A. (2020, feb). Ion-Neutral Collision Frequencies for Calculating Iono-
418 spheric Conductivity. *Journal of Geophysical Research: Space Physics*,
419 125(2). Retrieved from [https://onlinelibrary.wiley.com/doi/10.1029/](https://onlinelibrary.wiley.com/doi/10.1029/2019JA027128)
420 [2019JA027128](https://onlinelibrary.wiley.com/doi/10.1029/2019JA027128) doi: 10.1029/2019JA027128
- 421 Larsen, M. F. (2002, aug). Winds and shears in the mesosphere and lower ther-
422 mosphere: Results from four decades of chemical release wind measurements.
423 *Journal of Geophysical Research: Space Physics*, 107(A8), SIA 28–1–SIA 28–
424 14. Retrieved from <http://doi.wiley.com/10.1029/2001JA000218> doi:
425 10.1029/2001JA000218
- 426 Laundal, K. M. (2023). *Pure python international geomagnetic reference field (ppi-*
427 *grf)*. Retrieved from <https://github.com/klaundal/ppigrf> doi: 10.5281/
428 zenodo.5962660
- 429 Laundal, K. M., Reistad, J. P., Hatch, S. M., Madelaire, M., Walker, S., Hovland,
430 A. Ø., ... Sorathia, K. A. (2022, may). Local Mapping of Polar Iono-
431 spheric Electrodynamics. *Journal of Geophysical Research: Space Physics*,
432 127(5). Retrieved from [https://onlinelibrary.wiley.com/doi/10.1029/](https://onlinelibrary.wiley.com/doi/10.1029/2022JA030356)
433 [2022JA030356](https://onlinelibrary.wiley.com/doi/10.1029/2022JA030356) doi: 10.1029/2022JA030356

- 434 Liu, H., Bardeen, C. G., Foster, B. T., Lauritzen, P., Liu, J., Lu, G., ... Wang,
435 W. (2018, 2). Development and validation of the whole atmosphere com-
436 munity climate model with thermosphere and ionosphere extension (waccm-x
437 2.0). *Journal of Advances in Modeling Earth Systems*, 10, 381-402. doi:
438 10.1002/2017MS001232
- 439 Lu, G., Richmond, A. D., Emery, B. A., & Roble, R. G. (1995, oct). Magnetosphere-
440 ionosphere-thermosphere coupling: Effect of neutral winds on energy trans-
441 fer and field-aligned current. *Journal of Geophysical Research: Space*
442 *Physics*, 100(A10), 19643-19659. Retrieved from [http://dx.doi.org/](http://dx.doi.org/10.1029/95JA00766)
443 [10.1029/95JA00766](http://dx.doi.org/10.1029/95JA00766) <http://doi.wiley.com/10.1029/95JA00766> doi:
444 10.1029/95JA00766
- 445 Mannucci, A. J., McGranaghan, R., Meng, X., & Verkhoglyadova, O. P. (2022, nov).
446 An Analysis of Magnetosphere-Ionosphere Coupling That Is Independent of
447 Inertial Reference Frame. *Journal of Geophysical Research: Space Physics*,
448 127(11). Retrieved from [https://onlinelibrary.wiley.com/doi/10.1029/](https://onlinelibrary.wiley.com/doi/10.1029/2021JA030009)
449 [2021JA030009](https://onlinelibrary.wiley.com/doi/10.1029/2021JA030009) doi: 10.1029/2021JA030009
- 450 Matsuo, T. (2020). Recent progress on inverse and data assimilation procedure for
451 high-latitude ionospheric electrodynamics. In (p. 219-232). Springer Interna-
452 tional Publishing. Retrieved from [http://link.springer.com/10.1007/978-](http://link.springer.com/10.1007/978-3-030-26732-2_10)
453 [3-030-26732-2_10](http://link.springer.com/10.1007/978-3-030-26732-2_10) doi: 10.1007/978-3-030-26732-2_10
- 454 Merkin, V. G., & Lyon, J. G. (2010, oct). Effects of the low-latitude ionospheric
455 boundary condition on the global magnetosphere. *Journal of Geophysical Re-*
456 *search: Space Physics*, 115(A10). Retrieved from [http://doi.wiley.com/10](http://doi.wiley.com/10.1029/2010JA015461)
457 [.1029/2010JA015461](http://doi.wiley.com/10.1029/2010JA015461) doi: 10.1029/2010JA015461
- 458 Mesquita, R. L. A. (2021). *An Observational Investigation of Mid-Latitude*
459 *Thermospheric Temperatures and High-Latitude E-Region Neutral Wind*
460 *Structures* (Dissertation, Clemson University). Retrieved from [https://](https://tigerprints.clemson.edu/all_dissertations/2802/)
461 tigerprints.clemson.edu/all_dissertations/2802/
- 462 Mukhopadhyay, A., Jia, X., Welling, D. T., & Liemohn, M. W. (2021, 4). Global
463 magnetohydrodynamic simulations: Performance quantification of magne-
464 topause distances and convection potential predictions. *Frontiers in Astronomy*
465 *and Space Sciences*, 8. doi: 10.3389/fspas.2021.637197
- 466 Palmroth, M., Grandin, M., Sarris, T., Doornbos, E., Tourgaidis, S., Aikio, A., ...
467 Yamauchi, M. (2021, 2). Lower-thermosphere-ionosphere (lti) quantities:
468 current status of measuring techniques and models. *Annales Geophysicae*, 39,
469 189-237. Retrieved from [https://angeo.copernicus.org/articles/39/189/](https://angeo.copernicus.org/articles/39/189/2021/)
470 [2021/](https://angeo.copernicus.org/articles/39/189/2021/) doi: 10.5194/angeo-39-189-2021
- 471 Parker, E. N. (2007). *Conversations on Electric and Magnetic Fields in the Cosmos*.
472 Princeton University Press. Retrieved from [https://www.jstor.org/stable/](https://www.jstor.org/stable/10.2307/j.ctt2111gdt)
473 [10.2307/j.ctt2111gdt](https://www.jstor.org/stable/10.2307/j.ctt2111gdt) doi: 10.2307/j.ctt2111gdt
- 474 Qian, L., Burns, A. G., Emery, B. A., Foster, B., Lu, G., Maute, A., ... Wang,
475 W. (2014, 3). The near tie-gcm. In (p. 73-83). John Wiley & Sons,
476 Ltd. Retrieved from [https://onlinelibrary.wiley.com/doi/10.1002/](https://onlinelibrary.wiley.com/doi/10.1002/9781118704417.ch7)
477 [9781118704417.ch7](https://onlinelibrary.wiley.com/doi/10.1002/9781118704417.ch7) <http://dx.doi.org/10.1002/9781118704417.ch7> doi:
478 10.1002/9781118704417.ch7
- 479 Richmond, A. D. (1995). Ionospheric Electrodynamics Using Magnetic Apex Coordi-
480 nates. *Journal of geomagnetism and geoelectricity*, 47(2), 191-212. doi: 10
481 .5636/jgg.47.191
- 482 Richmond, A. D., & Kamide, Y. (1988). Mapping electrodynamic features of the
483 high-latitude ionosphere from localized observations - Technique. *Journal of*
484 *Geophysical Research*, 93(A6), 5741-5759. doi: 10.1029/JA093iA06p05741
- 485 Sangalli, L., Knudsen, D. J., Larsen, M. F., Zhan, T., Pfaff, R. F., & Rowland,
486 D. (2009, apr). Rocket-based measurements of ion velocity, neutral
487 wind, and electric field in the collisional transition region of the auroral
488 ionosphere. *Journal of Geophysical Research: Space Physics*, 114(A4).

- 489 Retrieved from <http://doi.wiley.com/10.1029/2008JA013757> doi:
490 10.1029/2008JA013757
- 491 Sarris, T. E. (2019, 7). Understanding the ionosphere thermosphere re-
492 sponse to solar and magnetospheric drivers: status, challenges and open
493 issues. *Philosophical Transactions of the Royal Society A: Mathemati-*
494 *cal, Physical and Engineering Sciences*, 377, 20180101. Retrieved from
495 <https://royalsocietypublishing.org/doi/10.1098/rsta.2018.0101>
496 doi: 10.1098/rsta.2018.0101
- 497 Weimer, D., & Edwards, T. (2021, jan). Testing the electrodynamic method to de-
498 rive height-integrated ionospheric conductances. *Annales Geophysicae*, 39(1),
499 31–51. Retrieved from [https://angeo.copernicus.org/articles/39/31/](https://angeo.copernicus.org/articles/39/31/2021/)
500 2021/ doi: 10.5194/angeo-39-31-2021